Development Of An Artificial Membrane Lung

by

Uditha Piyumindri Fernando

A dissertation submitted in partial fulfillment
of the requirements for the degree of
Doctor of Philosophy
(Biomedical Engineering)
in the University of Michigan
2017

Doctoral Committee:

Emeritus Professor Robert H. Bartlett, Co-Chair
Professor Joseph L. Bull, Co-Chair
Associate Professor William R. Lynch
Professor Mark E. Meyerhoff
Associate Professor Parag G. Patil

Acknowledgements

I would like to thank my committee for all their support and guidance throughout this process; you have each made an invaluable contribution to the progress of this project and my professional growth. I would especially like to thank my advisors, Dr. Bartlett and Dr. Bull, for their unfailing help, constant encouragement, and amazing foresight, which have been critical to this research as well as my professional life. They have been the foundation of my inspiration throughout this project. Thank you—for everything.

I would also like to thank all my mentors and colleagues in the ECLS lab, including Alvaro, Cindy, Marie, JT, Terry, Dr. Hirschl, Dr. Potkay, Alex, Liz, Nikki, Megan, Joe C, Ben, Jenn, Mere, Hannah, Hayley, Tommy, Fares, Elena, Alice, Jake, and Joe P, as well as my colleagues in the Biotransport lab: John, David, and Robinson—you, along with all other countless PIs, fellows, techs, and students have helped me immeasurably along the way, for which I am grateful. You have not only played a vital role in this research, but also have been my family away from home. To my colleagues in Aachen: Jutta, Andy, Felix, Peter, Georg, and Lotte—without you, this research would not be where it is today. Not only has your thoughtful help been vital in overcoming many critical obstacles in building lungs, but also the warm welcome you extended during my stay in Aachen has given me fond memories I will carry with

me for life.

To my undergraduate mentors at Yale, including Dr. Saltzman, Master Laurans, Dr. Batista, as well as my mentors at the Max Planck Institute in Goettingen: Dr. Hell, and Dr. Eggeling: I am forever grateful for the opportunities and guidance you provided me and thank you for fostering in me academic curiosity. To my dear friend, Eli: thank you for being my constant pillar of support throughout my time in Ann Arbor. You continue to inspire me to challenge the status quo in all facets of life. To Chad, who has enriched my life in ways he may not realize: thank you for your love. Your patience, ever-available support, and much-needed calming influence have sustained me in even the most trying times these last few years. Without you, I may never have finished this dissertation.

Most importantly, I would like to thank my family, to whom I owe everything. Ammi, Thathi, and Aiya, your constant love, encouragement, and confidence from afar has powered me through all my life, and this work is dedicated to you.

Table of Contents

List of Figures

List of Tables

ABSTRACT

Development Of An Artificial Membrane Lung

by

Uditha Piyumindri Fernando

Co-chair: Robert H. Bartlett

Co-chair: Joseph L. Bull

End-stage lung disease due to chronic obstructive pulmonary disease (COPD) is a leading cause of death across the world. However, treatment options for end-stage COPD are extremely limited. An artificial membrane lung designed to provide pulmonary support, primarily by clearance of CO_2, is a promising alternative treatment for end-stage COPD patients. Current hollow fiber membrane lungs feature a predominantly straight blood path length across the fiber bundle, resulting in limited oxygen transfer efficiency due to the boundary layer effect. Furthermore, these lungs also utilize long gas fibers relative to the blood path length, resulting in a limited CO_2 clearance efficiency due to the build-up of CO_2 within the fiber lumens.

Using computational fluid dynamics and optical flow visualization methods, a unique hollow fiber membrane lung was designed and created comprising concentric circular blood flow paths connected by gates, in addition to a short gas path length, referred to as the M-Lung. The M-Lung, comprising a fiber surface area of 0.28 m^2 and priming volume of 47 mL, has a rated flow of 2 L/min and the oxygenation efficiency is 357 $mL/min/m^2$. The CO_2 clearance of the lung is 200 mL/min at the rated blood flow. Given its high gas transfer efficiency, as well as its compact size, low priming volume, and propensity for minimal thrombogenecity, this lung design has the potential to be used in a range of acute and chronic respiratory support applications, including providing CO_2 clearance and partial oxygenation in adults with end-stage COPD as well as total respiratory support for infants and small children.

Chapter 1

Introduction

Motivations and Objectives

End-stage lung disease due to chronic obstructive pulmonary disease (COPD) is the third leading cause of death in the United States, and affects over 12 million adults each year. In addition, COPD inflicts a significant national economic burden, costing $50 billion in 2010 in direct and indirect costs[1]. COPD is a term that encompasses both chronic bronchitis and emphysema. These two diseases are characterized by obstruction to airflow that interferes with normal breathing. End-stage COPD, defined as Global Initiative for Chronic Obstructive Lung Disease (GOLD) stage 4: very severe[2], is characterized by progressively worsening CO_2 retention and concomitant dyspnea during activities of daily living, and finally even at rest, resulting in a severely diminished quality of life. Concomitantly, the clinical and economic cost of COPD increases with the severity of the disease, with end-stage COPD requiring the by far largest proportion of health-care resources due to excessive hospitalization, exacerbation and mortality rates[3-5]. The only currently available curative therapy for end-stage COPD is lung transplantation[6-9]. The demand for lungs, however, far exceeds the donor supply, resulting in long wait-times and ineligibility[8-10]; in 2011, COPD accounted for over 140,000 deaths, while fewer than 2000 lung transplants

were performed in the United States, including transplants for conditions other than COPD[11, 12]. The median wait time for a lung transplant is 4 months, and over 15% of patients die while awaiting a transplant[13]. Further, many other patients suffering from COPD may not be eligible for transplantation due to comorbidities or functional status. Current alternative treatment options for management of COPD are pharmacological therapy (primarily bronchodilators and corticosteroids), pulmonary rehabilitation, oxygen therapy, ventilator support, and lung volume reduction surgery (LVRS)[2]. However, these have limited efficacy in end-stage COPD[2], do not address CO_2 retention, do not improve the quality of life[14], or are contraindicated for patients with severely impaired lung function or comorbidities[15, 16]. These limitations highlight the need for a better alternative treatment option for end-stage COPD that addresses stabilization of the chronic disease and prevention of acute exacerbation, while allowing the patient to maintain a better quality of life.

Extracorporeal support for oxygenation was first proposed in 1972 by Hill et al.[17], and in 1978, Kolobow et al. demonstrated the feasibility of extracorporeal support for CO_2 removal[18]. Traditionally, the extracorporeal circuit is comprised of a membrane oxygenator, through which blood is pumped using a mechanical pump, as shown in Figure 1.1[19]. While this circuit is effective in both oxygenating and removing CO_2 and resolving related symptoms, the use of a mechanical pump necessitates a stay in an intensive care unit for the duration of the treatment. In addition to limiting a patient's activity, this exposes the patients to an increased risk of nosocomial infections[20, 21]. Furthermore, the use of extracorporeal membrane oxygenators carries

the risk of complications such as thrombosis and hemolysis[22]. These risks effectively limit the use of traditional extracorporeal support as a long-term therapy for end-stage COPD patients.

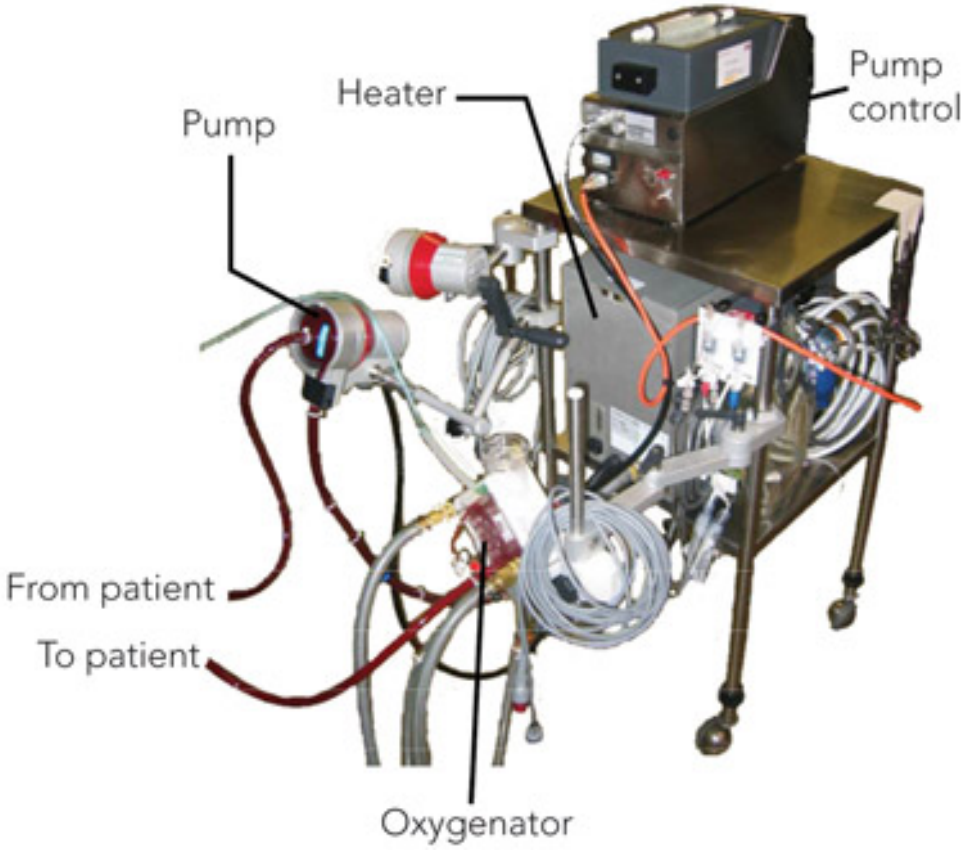

Figure 1.1: Standard extracorporeal membrane oxygenation circuit (taken from Lindstrom SJ, Pellegrino VA, Butt WW. Extracorporeal membrane oxygenation. The Medical journal of Australia. 2009;191(3):178-82.)

Coupled with recent advances in low-resistance membrane gas exchange devices, recent studies have demonstrated the feasibility of using pumpless extracorporeal CO_2 removal for treatment in acute respiratory distress syndrome (ARDS) or exacerbations with acute hypercapnic respiratory failure in COPD patients[23-25]. However, these pumpless circuits are still cumbersome and utilize oxygenators that

have less than optimally efficient performance, which restricts their potential for use as a long-term, ambulatory treatment in end-stage COPD. The objective of this study was to design a novel artificial lung that could be perfused by a systemic arterio-venous pressure gradient, to provide pulmonary support, primarily by clearance of CO_2, as a more effective long-term treatment option in end-stage COPD.

Artificial Membrane Lung Design

In the native lung, the low P_{CO_2} and high P_{O_2} in the alveolar space relative to adjacent capillary blood drives the diffusion of oxygen into blood and CO_2 out of blood (Figure 1.2A). In normal physiology, these concentration gradients are maintained through the process of breathing, referred to as ventilation, which removes the CO_2 build up in the alveolar space and reestablishes the gas concentration gradients. The process of exhaling is referred to as ventilation. Analogous to the gas exchange across the alveolar/capillary wall in the native human lung, gas exchange in hollow fiber membrane lungs is driven by the concentration gradient across the fiber membrane, which separates the blood and gas phases (Figure 1.2B).

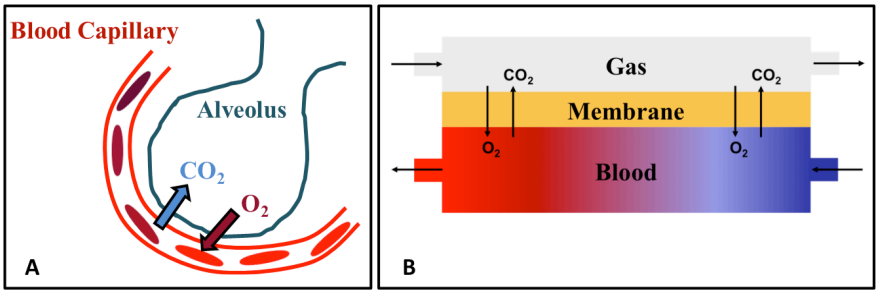

Figure 1.2: Diffusion driven gas exchange: A) across the alveolar/capillary wall in the native human lung and B) across the fiber membrane in hollow fiber membrane lungs.

In current hollow fiber membrane lungs, the primary blood path is straight flow directed across the fiber bundle. Only the red blood cells that are in contact with the gas exchange surface of each fiber are oxygenated; this is known as the diffusion boundary layer effect.[26] Mixing of the flowing blood to disrupt the boundary layer is achieved by the small secondary flows induced as the blood contacts each successive fiber.[27] This results in 100-160 mL oxygen exchange per minute per square meter at rated flow.[28] The rated flow is the flow of standardized venous blood that leaves the membrane lung at 95% oxyhemoglobin saturation. This project investigates the design and development of a novel paracorporeal M-Lung from the initial design phase through validation of the device in a large animal model.

The induction of secondary flows in a circular chamber, which could decrease the diffusion boundary layer effect, ultimately reaching the diffusion limit of the PDMS (silicone rubber) membrane, was described previously by Bartlett *et al*. and Drinker *et al*.[29-31] Blood was simulated by rapidly moving the membrane surface of the circular chamber against static or slowly flowing blood. A membrane lung using flat sheet PDMS formed into concentric circular chambers connected by gates, which reached membrane limitation for oxygen diffusion for PDMS. Secondary flows were created by mechanical oscillation of the device. The oxygen transfer efficiency was 205 $mL/min/m^2$ for a 5 mm PDMS membrane. The fabrication problems and noise made the design impractical for clinical use, but demonstrated that oxygen transfer efficiency is based on the extent of secondary flows.

Similar secondary flows are generated when blood flows through a static circular chamber with a curved flow path.[32, 33] The higher the flow, the more intense the secondary flow vortices formed. Therefore, we hypothesized that a membrane lung with concentric circular blood flow paths connected by gates would have high oxygenation efficiency created by secondary flows inherent in the design.

The physiological mechanism of CO_2 removal is distinct from that of oxygenation and therefore feature distinct optimal design criteria. While oxygenation is limited primarily by diffusion, CO_2 is limited primarily by ventilation. Hence, a key criterion of a lung designed for optimal CO_2 removal should be optimal ventilation. Clinically, CO_2 in enhanced by increasing the ventilation flow rate. However, the risk of fatal air emboli poses an upper limit to the ventilation flow rate. A more robust way of enhancing CO_2 ventilation is by maintaining short gas fibers. We therefore hypothesized that a membrane lung featuring short fibers (as opposed to fewer longer fibers) would have a high CO_2 removal efficiency as a result of minimizing CO_2 build-up in the gas phase. Based on these hypotheses, we designed a novel membrane lung, referred to as the M-Lung.

The M-Lung Design

The M-Lung design is shown in Figure 1.3. The device has an outer shell comprising a blood inlet port, blood outlet port, gas inlet port, and gas outlet port (Figure 1.3A*).

* A full International Patent Application has been filed for the M-Lung design on behalf of the Regents of the University of Michigan through the University of Michigan Technology Transfer Office by Harness, Dickey & Pierce, P.L.C. The inventors listed are Robert H. Bartlett, Joseph L. Bull, and Uditha Piyumindri Fernando.

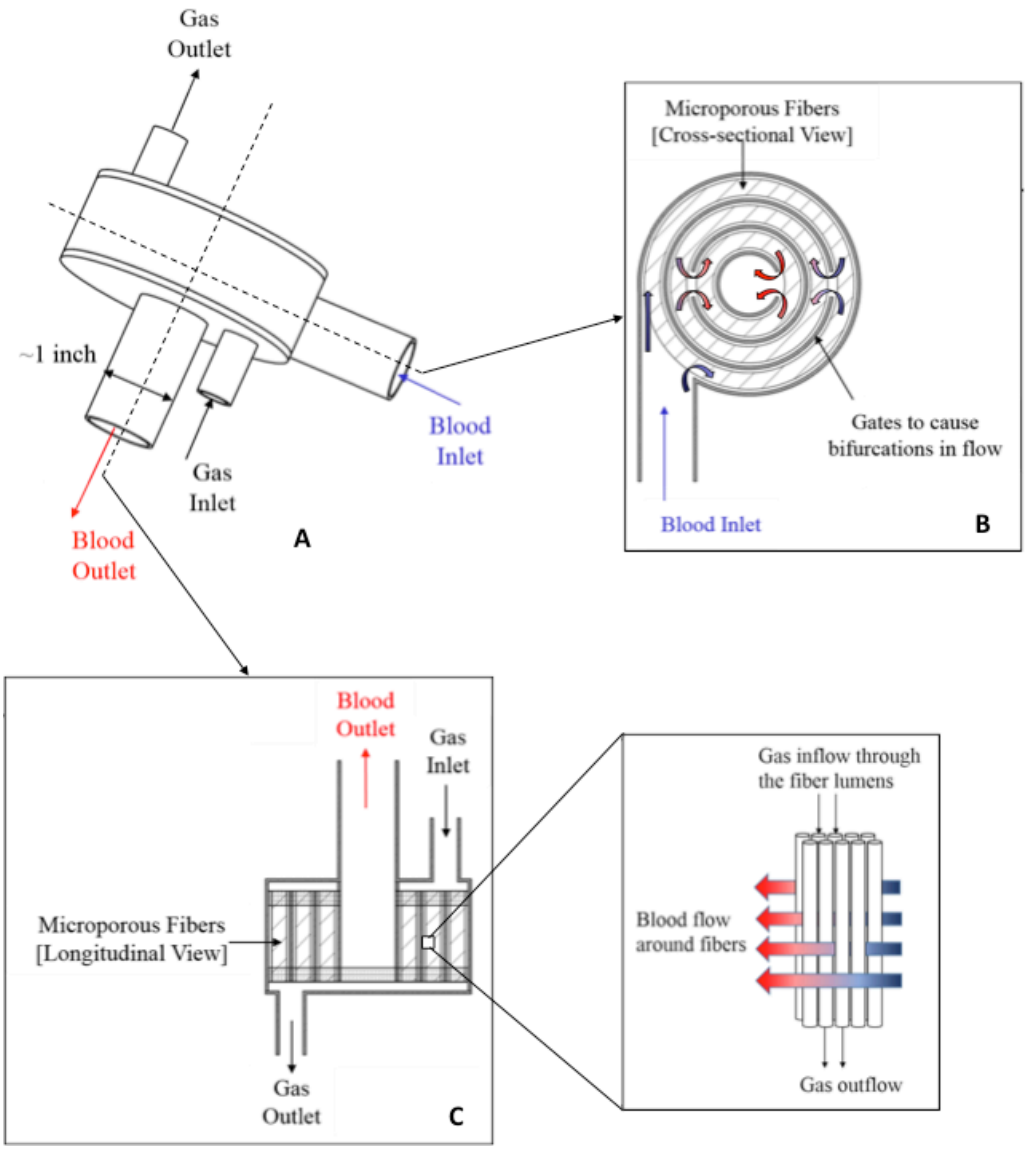

Figure 1.3: M-Lung design. Cross sectional views of the assembled device (A) is shown in B and C. The colored arrows indicate the concentration levels of O_2 and CO_2 in blood: red indicates blood with high O_2 and low CO_2 concentrations, while blue indicates blood with low O_2 and high CO_2 concentrations.

Blood with low O_2 and high CO_2 concentrations (systemic venous blood) enters the blood inlet port lumen, and blood with high O_2 and low CO_2 concentrations exits the M-Lung through the blood outlet port. Air with high O_2 and low CO_2 concentrations is introduced in via gas inlet port and a mixture of low O_2 and high CO_2

concentrations exits the M-Lung via gas outlet port lumen, as shown in Figure 1.3A,C. As shown in Figure 1.3B, the oxygenator outer shell encloses a fiber bundle and a number of circular dividers radially separating the fiber bundle. Each divider has a single gate opening, allowing the blood to flow through the fiber bundle compartments; the blood from the blood inlet port flows through the fiber bundle compartments into the lumen of the blood outlet port. The fiber bundle (Figure 1B,C) comprises an array of micro-porous hollow fibers having the upper and lower ends potted, so that the lumens of the fibers communicate with plenum between the gas ports and the fiber bundle. The fiber bundle is wound around the innermost divider such that the cross section of each fiber is parallel to the cross-sectional plane in Figure 1.3B.

Summary Of The Study

The goal of this work was to design and build a novel, highly efficient, and compact artificial lung that could be perfused by the heart (via systemic arterio-venous pressure gradient), which had the potential to serve as a more effective long-term treatment option in end-stage COPD. Computational and experimental methods were used to develop the lung from the initial design phase through validation of the device *in vitro*. First, the design concept is developed and the underlying fluid dynamics is investigated both theoretically and experimentally. Next, we the functional performance of the M-Lung is tested *in vitro*. Finally, the functional efficiency of the M-Lung is compared to similarly sized commercial oxygenators.

References

1. Guarascio AJ, Ray SM, Finch CK, Self TH. The clinical and economic burden of chronic obstructive pulmonary disease in the USA. ClinicoEconomics and outcomes research : CEOR. 2013;5:235-45.

2. Global Strategy For The Diagnosis, Management, And Prevention Of Chronic Obstructive Pulmonary Disease. 2014.

3. Chapman KR, Mannino DM, Soriano JB, Vermeire PA, Buist AS, Thun MJ, et al. Epidemiology and costs of chronic obstructive pulmonary disease. The European respiratory journal. 2006;27(1):188-207.

4. Budweiser S, Jorres RA, Pfeifer M. Treatment of respiratory failure in COPD. International journal of chronic obstructive pulmonary disease. 2008;3(4):605-18.

5. Ambrosino N, Simonds A. The clinical management in extremely severe COPD. Respiratory medicine. 2007;101(8):1613-24.

6. Nathan SD. Lung transplantation: disease-specific considerations for referral. Chest. 2005;127(3):1006-16.

7. Lin YC, Brant DO, Bartlett RH, Hirschl RB, Bull JL. Pulsatile flow past a cylinder: an experimental model of flow in an artificial lung. ASAIO J. 2006;52(6):614-23.

8. Patel N, DeCamp M, Criner GJ. Lung transplantation and lung volume reduction surgery versus transplantation in chronic obstructive pulmonary disease. Proceedings of the American Thoracic Society. 2008;5(4):447-53.

9. Mora JI, Hadjiliadis D. Lung volume reduction surgery and lung transplantation in chronic obstructive pulmonary disease. International Journal of Chronic Obstructive Pulmonary Disease. 2008;3(4):629-35.

10. Janssen DJ, Spruit MA, Does JD, Schols JM, Wouters EF. End-of-life care in a COPD patient awaiting lung transplantation: a case report. BMC Palliative Care. 2010;9:6.

11. Hoyert DL, Xu J. Deaths: preliminary data for 2011. National vital statistics reports : from the Centers for Disease Control and Prevention, National Center for Health Statistics, National Vital Statistics System. 2012;61(6):1-51.

12. Data. Organ Procurement and Transplantation Network, U.S. Department of Health and Human Services Health Resources and Services Administration, 2011.

13. Annual Data Report of the US Organ Procurement and Transplantation Network (OPTN) and the Scientific Registry of Transplant Recipients (SRTR). Introduction. American journal of transplantation: official journal of the American Society of Transplantation and the American Society of Transplant Surgeons. 2013;13 Suppl 1:8-10.

14. McEvoy RD, Pierce RJ, Hillman D, Esterman A, Ellis EE, Catcheside PG, et al. Nocturnal non-invasive nasal ventilation in stable hypercapnic COPD: a randomised controlled trial. Thorax. 2009;64(7):561-6.

15. Fishman A, Martinez F, Naunheim K, Piantadosi S, Wise R, Ries A, et al. A randomized trial comparing lung-volume-reduction surgery with medical therapy for severe emphysema. The New England Journal of Medicine. 2003;348(21):2059-73.

16. Patients at high risk of death after lung-volume-reduction surgery. The New England journal of medicine. 2001;345(15):1075-83.

17. Hill JD, O'Brien TG, Murray JJ, Dontigny L, Bramson ML, Osborn JJ, et al. Prolonged extracorporeal oxygenation for acute post-traumatic respiratory failure (shock-lung syndrome). Use of the Bramson membrane lung. The New England journal of medicine. 1972;286(12):629-34.

18. Kolobow T, Gattinoni L, Tomlinson T, Pierce JE. An alternative to breathing. The Journal of thoracic and cardiovascular surgery. 1978;75(2):261-6.

19. Lindstrom SJ, Pellegrino VA, Butt WW. Extracorporeal membrane oxygenation. The Medical journal of Australia. 2009;191(3):178-82.

20. Witer LH, R.; Trahanas, J.; Bryner, B.; Hoffman, H.; Rojas, A.; Bartlett, R.; Lynch, W.;. Large Animal Model of a Pumpless Arteriovenous Extracorporeal CO2 Removal via Subclavian Vessels. 2014:[In Preparation].

21. Vincent JL, Bihari DJ, Suter PM, Bruining HA, White J, Nicolas-Chanoin MH, et al. The prevalence of nosocomial infection in intensive care units in Europe. Results of the European Prevalence of Infection in Intensive Care (EPIC) Study. EPIC International Advisory Committee. Jama. 1995;274(8):639-44.

22. Zwischenberger JB, Nguyen TT, Upp JR, Jr., Bush PE, Cox CS, Jr., Delosh T, et al. Complications of neonatal extracorporeal membrane oxygenation. Collective experience from the Extracorporeal Life Support Organization. The Journal of thoracic and cardiovascular surgery. 1994;107(3):838-48; discussion 48-9.

23. Lund LW, Federspiel WJ. Removing extra CO2 in COPD patients. Current respiratory care reports. 2013;2:131-8.

24. Cove ME, MacLaren G, Federspiel WJ, Kellum JA. Bench to bedside review: Extracorporeal carbon dioxide removal, past present and future. Crit Care. 2012;16(5):232.

25. Hamid IA, Hariharan AS, Shankar NR. The advent of ECMO and pumpless extracorporeal lung assist in ARDS. Journal of emergencies, trauma, and shock. 2011;4(2):244-50.

26. Peirce EC, Dibelius NR. Membrane Lung - Studies with a New High Permeability Co-Polymer Membrane. T Am Soc Art Int Org. 1968;14(Apr):220-&.

27. Zwischenberger JB, Anderson CM, Cook KE, Lick SD, Mockros LF, Bartlett RH. Development of an implantable artificial lung: challenges and progress. ASAIO journal. 2001;47(4):316-20.

28. Stanzel RD, Henderson M. Clinical evaluation of contemporary oxygenators. Perfusion. 2016;31(1):15-25.

29. Bartlett RH, Kittredge D, Noyes BS, Willard RH, Drinker PA. Development of a Membrane Oxygenator - Overcoming Blood Diffusion Limitation. J Thorac Cardiov Sur. 1969;58(6):795-+.

30. Drinker PA, Bartlett RH, Bialer RM, Noyes BS, Jr. Augmentation of membrane gas transfer by induced secondary flows. Surgery. 1969;66(4):775-81.

31. Benn JA, Drinker PA, Mikic B, Shults MC, Lacava EJ, Kopf GS, et al. Predictive Correlation of Oxygen and Carbon Dioxide Transfer in a Blood Oxygenator with Induced Secondary Flows. T Am Soc Art Int Org. 1971;17(Apr):317-&.

32. Berger SA, Talbot L, Yao LS. Flow in Curved Pipes. Annu Rev Fluid Mech. 1983;15:461-512.

33. Nandakumar K, Masliyah JH. Bifurcation in Steady Laminar-Flow through Curved Tubes. J Fluid Mech. 1982;119(Jun):475-90.

Chapter 2

M-Lung Design

Introduction

In Chapter 1, the basis for the M-Lung design is described; it was hypothesized that a membrane lung with concentric circular blood flow paths connected by gates would have high oxygenation efficiency created by secondary flows inherent in the design, while a membrane lung featuring short fibers would have a high CO_2 removal efficiency as a result of minimizing CO_2 build-up in the gas phase. In this chapter, the flow dynamics within the M-Lung is evaluated using both computational and optical visualization methods to understand the effect of design parameters on flow dynamics and optimize the design of the M-Lung. `

Methods

Computational Fluid Dynamics

In order to evaluate and optimize flow patterns through the M-Lung housing, the flow through the M-Lung housing was simulated both with and without the fiber bundle, for a variety of models with varying gate widths, numbers of gates, and placements, and inlet flow rates. The following parameters were evaluated: velocity, vorticity, pressure drop, resistance, shear stress, circulation, fiber surface area, and priming volume. SolidWorks (Dassault Systèmes SolidWorks Corp., Concord, MA) and Creo

(PTC Inc., Needham, MA) computer-aided design (CAD) software was used to create each model, which was then imported into the COMSOL Multiphysics (COMSOL AB, Stockholm, Sweden) CFD software program. Blood was modeled as an incompressible Newtonian fluid governed by equations 1-2.

$$\rho(u \cdot \nabla)u = \nabla \cdot [-pI + \mu(\nabla u + (\nabla u)^T)] \quad (1)$$

$$\rho \nabla \cdot u = 0 \quad (2)$$

Where μ denotes the dynamic viscosity (Pa·s), u denotes the velocity (m/s), ρ is the fluid's density (kg/m^3), and p is the pressure (Pa). For blood, ρ and μ were set to be 1060 kg/m^3 and 0.003 Pa s, respectively. The boundary conditions were set as follows: wall = no slip, inlet = pulsatile flow (frequency = 1 Hz, amplitude = 2 x average flow rate [1.3 L/min and 3 L/min], waveform = sinusoidal, as shown in Figure 2.1), and outlet = atmospheric pressure.

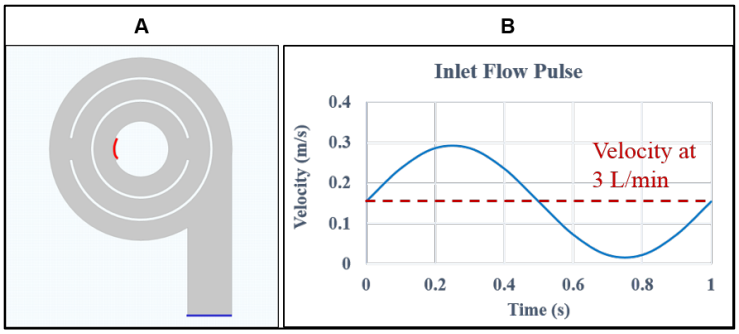

Figure 2.1: Inlet boundary conditions for CFD. The inlet (blue) and outlet (red) boundaries are shown in A, and the pulsatile flow at the inlet for an average flow of 3 L/min is illustrated in B.

A finite element formulation based on the Galerkin method was used to solve for the governing equations. The convergence criterion was set to be a relative tolerance of 0.001 and 0.01 for stationary and time-dependent solutions, respectively. The velocity, vorticity, and pressure of the flow are found directly using the software, while resistance, shear stress, and circulation are calculated as given in Eq. 3-5, where r denotes resistance (Ω), Q denotes volumetric flow rate (m^3/s), τ denotes shear stress (Pa), $\dot{\gamma}$ denotes shear rate (1/s), C denotes circulation, and ν denotes vorticity (1/s):

$$r = \frac{\Delta p}{Q} \tag{3}$$

$$\tau = \mu\dot{\gamma} \tag{4}$$

$$C = \iint \nu \, dS \tag{5}$$

In addition, the hollow membrane fiber bundle was incorporated into our model as a porous media, governed by Darcy's law with the Brinkman and Forchheimer extensions, shown in Eq. 6-9. [1, 2] The Brinkman extension accounts for momentum transport by macroscopic viscous effects as well as pressure gradients, while the Forchheimer extension accounts for the turbulent contribution to the resistance to flow in the porous domain.

$$\frac{\mu}{\kappa}u = \nabla \cdot \left[-pI + \frac{\mu}{\epsilon_P}(\nabla u + (\nabla u)^T)\right] - \beta_F |u| u \tag{6}$$

$$\nabla \cdot u = 0 \tag{7}$$

Where κ denotes the permeability of the porous medium (m^2), ϵ_P is the porosity (dimensionless), and β_F, the Forchheimer coefficient, is given by Eq. 9, where C_F is the dimensionless friction coefficient (Eq. 8).

$$C_F = \frac{1.75}{\sqrt{150{\epsilon_P}^3}} \tag{8}$$

$$\beta_F = \frac{\rho \epsilon_P C_f}{\sqrt{\kappa}} \tag{9}$$

The effects of varying the fiber bundle density were studied by varying the permeability of the porous medium. The permeability and porosity of the fiber bundle region is related to the total fiber surface area, A_{fiber} (m^2), as shown in Eq. 10-12[3-5]:

$$\kappa = \frac{{\epsilon_P}^3 {d_{HFM}}^2}{150(1-\epsilon_P)^2} \tag{10}$$

$$\epsilon_P = 1 - \frac{N_{fiber} {d_{HFM}}^2}{{D_o}^2 - {D_i}^2} \tag{11}$$

$$A_{fiber} = \pi d_{HFM} H N_{fiber} \tag{12}$$

Where d_{HFM} denotes the fiber membrane outer diameter (m), N_{fiber} is total number of fibers, D_i and D_o are the inner and outer diameter of each fiber bundle, and H is the height of the fibers.

Particle Image Velocimetry

In order to verify simulated flow patterns through the M-Lung housing, optical visualization of flow patterns through the M-Lung were carried out using particle image velocimetry (PIV). The experimental setup is shown in Figure 2.2.

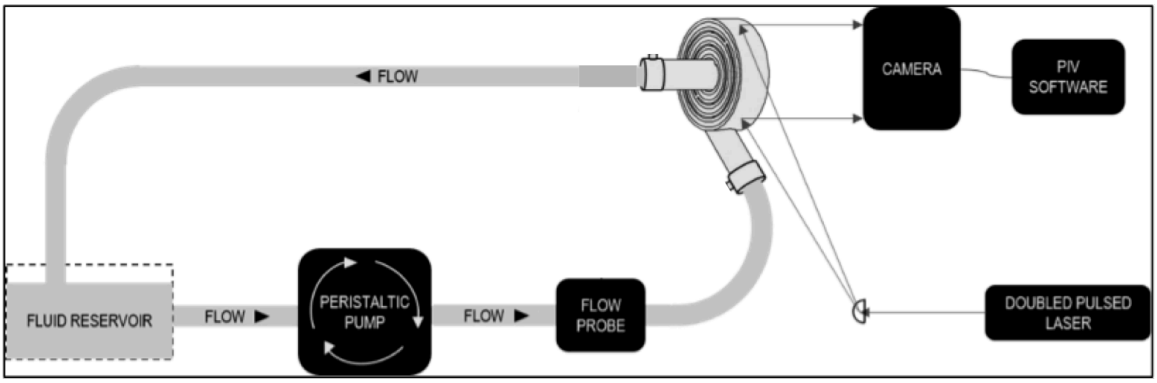

Figure 2.2: Particle image velocimetry setup. The grey arrows indicate the laser path, which originates from the laser source, is shaped into a laser sheet through a cylindrical lens, and illuminates a slice of the M-Lung device.

The M-Lung prototype comprised a poly(methyl methacrelate) (PMMA) housing. De-ionized water was used as the model fluid to represent the blood in these experiments, since it provided sufficient optical clarity for the particle velocimetry measurements described below. Fluid through the M-Lung was pumped using a peristaltic pump set to flow rates of 1.5 L/min and 3.0 L/min to match the inlet flow rates used in CFD simulations. The water was seeded with neutrally buoyant micro-porous round polyamide seeding particles (diameter = 20 μm, density = 1.03 g/m^3, Dantec Dynamics Co., Skovlunde, Denmark). These particles were illuminated by a pulsed Nd-YAG laser light (Model: Solo III 15Hz, No: 16155, wavelength 532 nm, New Wave Inc., Fremont, CA, U.S.) as shown in Figure 3.2. The laser's beam passed

through a cylindrical lens (Modular Focus, f=-6mm, Rodenstock Co., Munich, Germany) and then shaped into a laser light sheet (<1 mm thickness and 100 mm in width) that illuminated the area of interest. The images were captured by a CCD camera (Flowmaster 3S. resolution: 1280x1024 pixels, LaVision Inc., Goettingen, Germany), which was positioned as shown in Figure 2.2. Successive pairs of single exposed images were then processed employing PIV software (Davis 6.2, LaVision Inc., Goettingen, Germany). Each of the images was divided into small interrogation areas of 32x32 pixels, and was cross-correlated with each other with a 50% overlap. A time sequence of the velocity field was obtained by capturing successive pairs of images and repeating the image cross correlations. The experimental velocity field images were then compared with previously obtained computational velocity fields through the M-Lung housing (without fibers).

Results

Computational Fluid Dynamics

The CFD results, as shown in Figure 2.3, show a well-distributed blood flow profile through the device with minimal regions of low blood flow and demonstrate the formation of transient flow vortices through the M-Lung housing. The resulting flows predict that increasing the flow rate at the inlet increases the mixing, pressure drop, and resistance across the device. Furthermore, increasing the number of gates also results in an increased velocity (since the effective flow path is elongated), mixing, pressure drop, and resistance across the device.

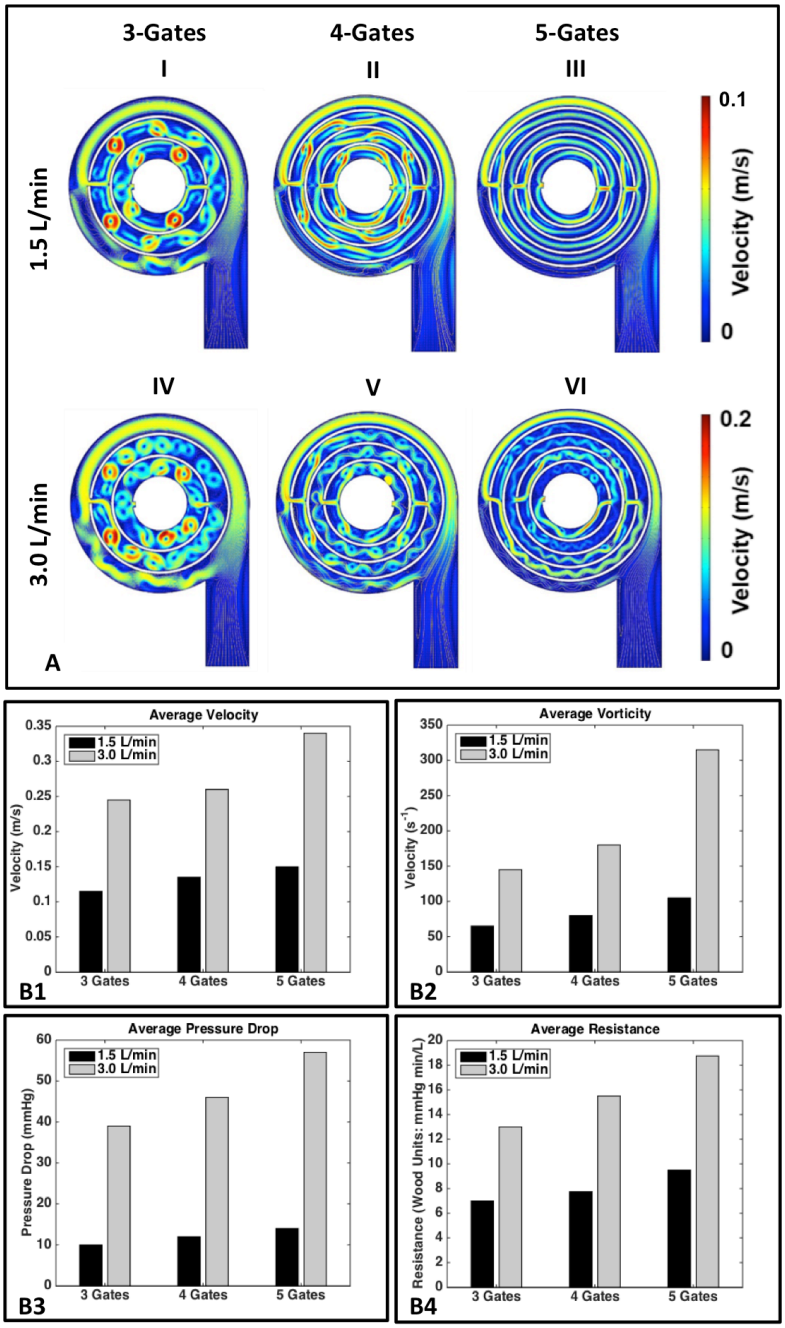

Figure 2.3: Varying number of gates and inlet flow rate. (A) illustrates flow patterns at t = 4.75 s for an inlet flow rate of 1.5 L/min (I-III) and 3 L/min (IV-VI), with 3 gates (I,IV), 4 gates (II,V), and 5 gates (III,VI), and the corresponding velocity streamlines shown by the yellow lines. (B) shows the corresponding velocity (B1), vorticity (B2), pressure drop (B3), and resistance (B4), averaged across 5 seconds.

Next, the fiber bundle was incorporated into the 3-gate model and varied gate width (the width of each gate is the distance between the edges of the opening arc of divider

placed at a given radial distance). The resulting flow dynamics show that increasing the gate width increases the shear stress (Figure 2.4A) and circulation (Fig. 2.4B) across the device.

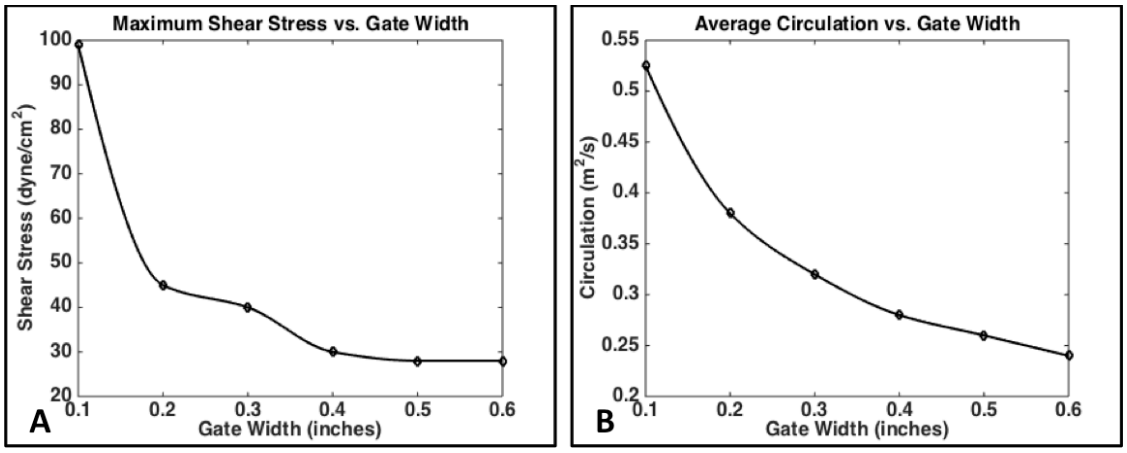

Figure 2.4: Computational flow dynamics for varying gate width. The maximum shear stress (A) and circulation (B) averaged across 5 seconds is shown as a function of gate opening width; the fiber bundle permeability (k) = $2.8e^{-5}$ m^2.

Thereafter, we studied the effects of varying permeability of the porous media, which relates to the fiber bundle packing density and fiber surface area as given in Eq. 5-7. The resulting flow patterns (Figure 2.5A) show that the vortices formed in the M-Lung housing are dampened by the membrane fiber bundle, with the magnitude of dampening dependent on the permeability of the membrane fiber bundle (Figure 2.5B); decreasing the permeability increases the mixing, shear stress (Figure 2.5B,D), and circulation (Figure 2.5C,D) across the device, while decreasing the shear stress and vorticity at the gates (Figure 2.5D).

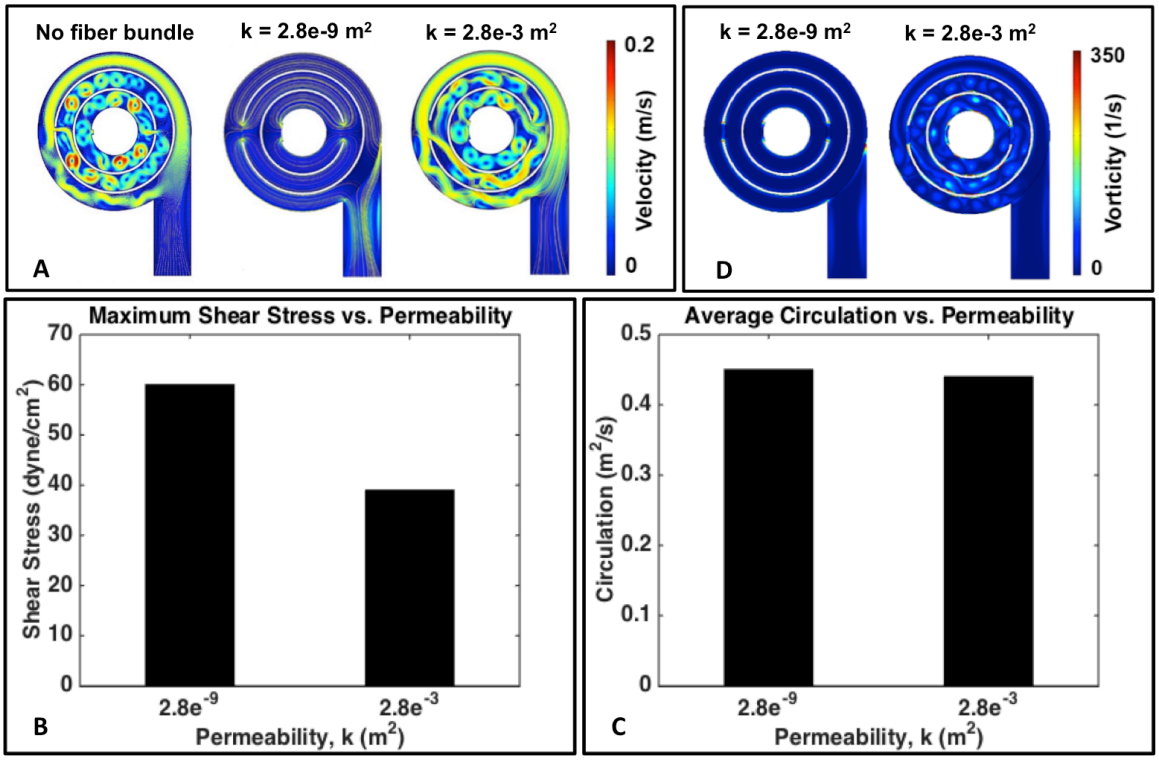

Figure 2.5: Computational flow patterns for varying fiber bundle permeability. (A) shows the velocity profiles obtained at t = 4.75 s for varying fiber bundle permeability (k). The yellow lines denote velocity streamlines. The maximum shear stress (B) and circulation (C) averaged across 5 seconds is shown as a function of permeability.

The permeability of the fiber bundle can be modulated in the fabrication process by varying the number of fibers/cm and/or the spacing between each layer of fibers. The relationship between fiber bundle permeability and simulated M-Lung pressure drop, priming volume, and fiber surface area is shown in Figure 2.6A-C. The simulations demonstrate that a significant reduction in the pressure drop across the M-Lung could be achieved increasing the fiber bundle permeability (Figure 2.6A), at the cost of an increased priming volume (Figure 2.6B) and reduced fiber surface area (Figure 2.6A).

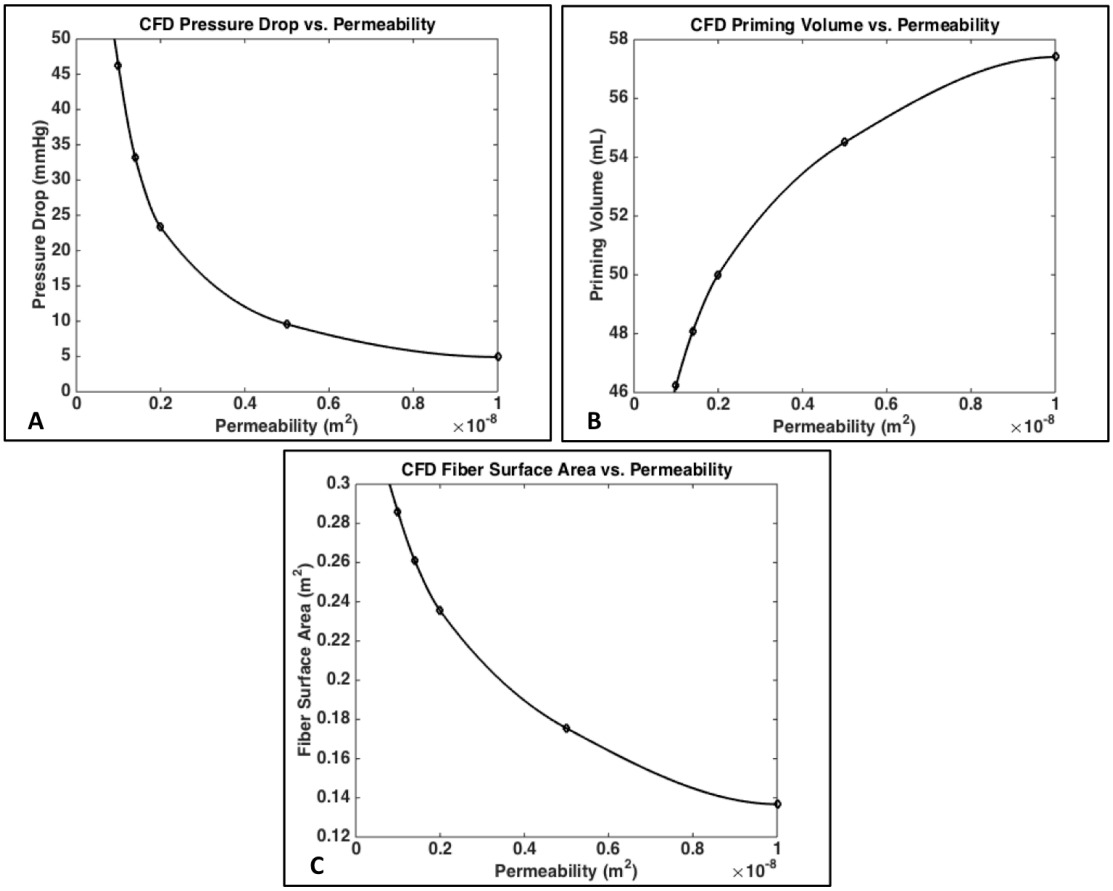

Figure 2.6: Simulated effects of varying fiber bundle permeability on M-Lung pressure drop for Q_b = 0.5 L/min (A), priming volume (B), and fiber surface area (C).

Particle Image Velocimetry

A comparison of the flow through the M-Lung obtained using simulations and optical flow visualization is shown in Figure 2.7. The PIV results demonstrate similar flow patterns to those obtained computationally; we observe transient vortices forming immediately both experimentally (Figure 2.7A) and computationally (Figure 2.7B) after the fluid passes through the gate of the concentric divider.

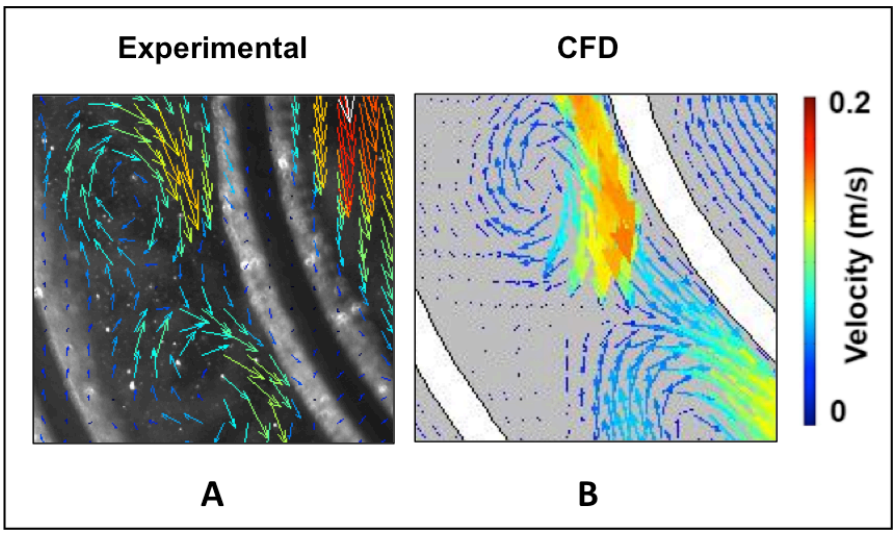

Figure 2.7: Comparison of simulated and experimental flow through the M-Lung housing. The experimental PIV results (A) demonstrate similar flow patterns to those obtained computationally (B).

Discussion

The CFD results show a well-distributed blood flow profile through the M-Lung with minimal regions of low blood flow. The results also demonstrate the formation of transient flow vortices through the M-Lung housing, suggesting that the gated design promotes passive secondary flow mixing. Experiemental PIV results demonstrate a similar vortex pattern to those obtained computationally. While increasing the number of gates results in a longer effective blood path and increase in mixing, the resulting increase in resistance poses an upper limit to the number of gates that could be supported by systemic arterio-venous perfusion.

The mixing within the M-Lung housing is dampened by the membrane fiber bundle, with the magnitude of dampening dependent on the permeability of the membrane fiber bundle. The simulations demonstrate that an increase in secondary flow mixing

and a significant reduction in the pressure drop across the M-Lung could be achieved by increasing the fiber bundle permeability, at the cost of an increased priming volume and reduced fiber surface area.

The specific pattern of secondary flows generated depends on a variety of factors, including inlet flow rate and pulsatility and specific configuration of dividers and gates. Since the inlet flow rate and pulsatility are dependent on the perfusion system (pump or native circulation) variations of this design will incorporate a variety of divider and gate configurations to meet flow requirements.

In conclusion, using CFD and optical flow visualization methods, a unique hollow fiber membrane lung with passive secondary flow generation based on concentric circular blood flow paths connected by gates was designed and optimized. In prototype testing, flow patterns across the M-Lung matched those predicted by CFD. In the next chapter, a functional prototype of the optimal M-Lung design is built based on these simulations, and its performance is evaluated *in vitro*.

References

1. Amiri A, Vafai K. Transient analysis of incompressible flow through a packed bed. Int J Heat Mass Tran. 1998;41(24):4259-79.

2. Ergun S. Fluid Flow through Packed Columns. Chem Eng Prog. 1952;48(2):89-94.

3. Khanafer K, Cook K, Marafie A. The Role of Porous Media in Modeling Fluid Flow within Hollow Fiber Membranes of the Total Artificial Lung. J Porous Media. 2012;15(2):113-22.

4. Vafai K. Convective Flow and Heat-Transfer in Variable-Porosity Media. J Fluid Mech. 1984;147(Oct):233-59.

5. Vafai K. Analysis of the Channeling Effect in Variable Porosity Media. J Energ Resour-Asme. 1986;108(2):131-9.

Chapter 3

Membrane Lung Fabrication and Performance

Introduction

In Chapter 2, the flow dynamics within the M-Lung was evaluated using both computational and optical visualization methods and optimized the design of the M-Lung. In this chapter, functional prototypes of the M-Lung are built based on the optimized design and evaluated the functional performance of the M-Lung *in vitro*. The performance of the M-Lung is then compared to similarly sized commercial oxygenators in order to test our hypothesis that the unique M-Lung design comprising a concentric circular blood path and short gas path relative to blood path results in an increased efficiency of both oxygenation and CO_2 clearance.

Methods

A schematic of the CFD-optimized M-Lung is shown in Figure 3.1. The device has an outer shell comprising a blood inlet, blood outlet, gas inlet, and gas outlet ports, as shown in Figure 3.1A. This outer shell encloses a fiber bundle separated into compartments radially by concentric, circular dividers. Each divider has a gate opening, allowing the blood to flow through the fiber bundle compartments; the blood

from the blood inlet port flows through the fiber bundle compartments into the lumen of the blood outlet port. The fiber bundle comprises an array of micro-porous hollow fibers having the upper and lower ends potted, so that the interior lumens of the fibers communicate with plenum between the gas ports and the fiber bundle. The fiber bundle is wound around the concentric dividers such that the main direction of blood flow is perpendicular to direction of gas flow (Figure 3.1B).

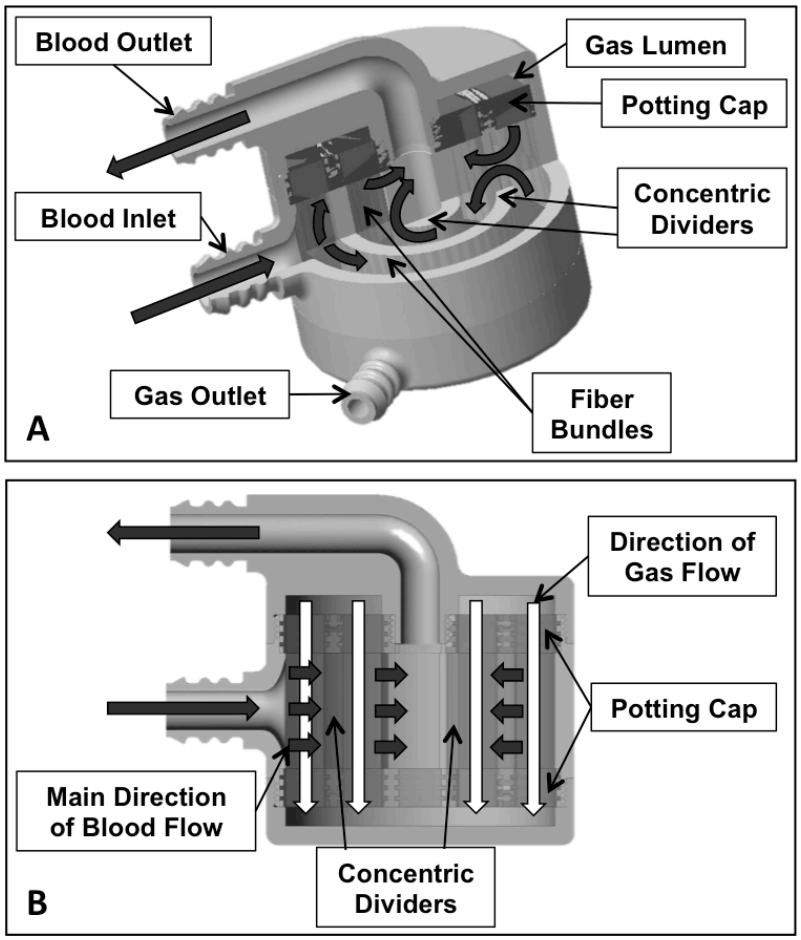

Figure 3.1: M-Lung design. Cross sectional views of the assembled device are shown in A and B. The black and white arrows indicate the main direction of blood flow and gas flow, respectively.

The specifications for the lung design were as follows: a rated flow ≥1 L/min, oxygen transfer at rated flow ≥50 mL/min, pressure drop at rated flow of 60 mmHg, and CO_2 clearance that is four times oxygen transfer. The specifications were chosen based on characteristics of existing commercial pediatric size membrane lungs for direct comparison among devices. Furthermore, a membrane lung with these specifications would provide total gas exchange for a 10 kg child and total systemic CO_2 removal for an adult. The following parameters were evaluated: rated flow, surface area, oxygen transfer efficiency, priming volume, pressure drop, and CO_2 clearance.

Prototype Fabrication

In order to evaluate the blood gas-exchange performance of the M-Lung, functional prototypes, shown in Figure 3.2, were fabricated as follows: The M-Lung housing was manufactured using stereolithography (Objet Eden 350v, material: photopolymer "Full Cure 720"), and the fiber bundle comprised a cross-wound mat (Figure 3.2A) of hollow micro-porous polypropylene (PP) membrane fibers (Membrana GmbH, Wuppertal, Germany) with 17 fibers/cm, resulting in a fiber bundle porosity of 0.63, fiber surface area of 0.28 m^2, fiber length of 2 cm, and priming volume of 47 mL. An in-house built centrifuge was used for potting each end of the M-Lung; the M-Lung housing, with with the wound fiber bundles and gates in place, were centrifuged at a speed of 800 RPM and temperature of 50^0C for 1 hour, following which the potted devices were allowed to cure at 50^0C for 24 hours. As potting material, a biocompatible, addition-curing silicone rubber (Wacker Chemie AG, Munich, Germany) was utilized, as shown in Figure 3.2B, C.

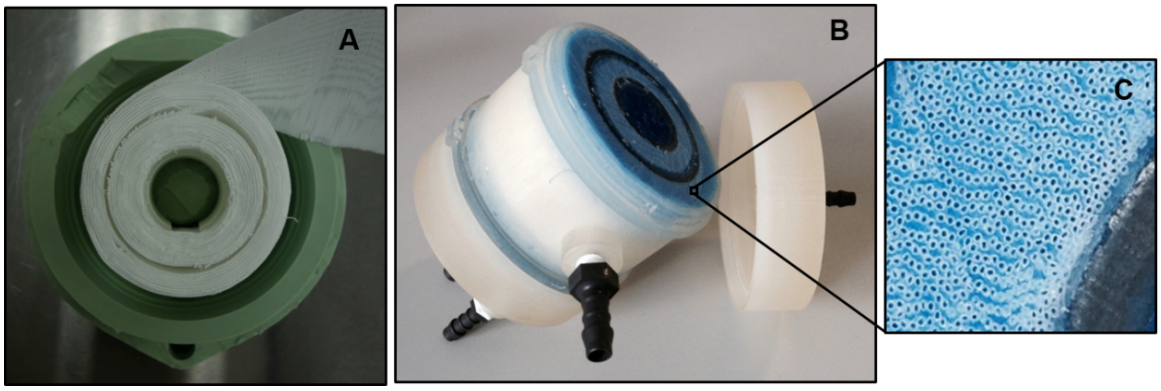

Figure 3.2: Manufacturing functional M-Lung prototypes. (A) shows the fiber mat wound with the divider in place, while (B) shows the assembled device. A zoomed-in view of the patent potted fibers is given in (C). The blue regions in (B) and (C) indicates the potting material.

In vitro Testing

The functional performance of the M-Lung was evaluated *in vitro* in accordance with the Food and Drug Administration Guidance for Cardiopulmonary Bypass Oxygenators 510(k) guidelines[1] using a test circuit as shown in Figure 3.3. Fresh bovine blood was anti-coagulated with heparin to obtain an activated clotting time (ACT) > 480 s and filtered through a 70-120 μm screen filter into a clean carboy. The circuit was primed and de-aired using a 0.9% sodium chloride (saline) solution, which was displaced by filtered blood from the filtration reservoir. The circuit total hemoglobin was measured and adjusted with saline solution to 12 ± 1 g/dL. Gas lines from the three gas flow controllers (O_2, N_2, and CO_2) were connected to the conditioning device (Novalung iLA, Xenios AG, Heilbronn, Germany), and the overall gas mixture was controlled by controlling the flow rate of these individual gases during the conditioning process. A flow probe (Transonic, Ithaca, NY) was used to monitor and control the blood flow rate through the circuit, while pressure

transducers were connected to the blood inlet and blood outlet sites of the test device to monitor the pressure drop across the M-Lung. A heat exchanger connected to the circuit was used to warm circuit blood to 37 ± 1 ºC. The blood was pumped and recirculated through the conditioning device until the blood pool reached venous conditions, as outlined in Table 3.1. The conditioned blood flow was then directed to the test device alone, and the outflow of the test device was directed to the second carboy, comprising a single pass test. The test device was ventilated using a sweep gas comprised of 100% O_2.

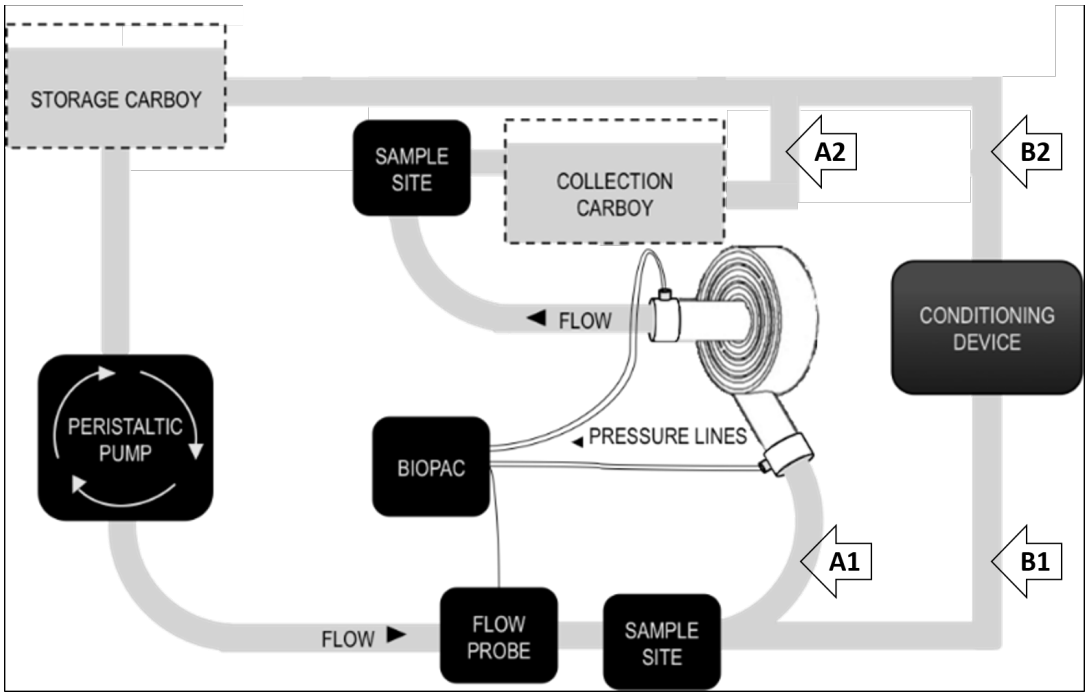

Figure 3.3: In vitro test circuit schematic. During the conditioning process, the test device is isolated from the circuit using clamps at the points denoted by arrows A1 and A2. During the testing process, the blood is directed through the test device alone and into a separate collection carboy using clamps at points denoted by arrows A2, B1, and B2, thereby comprising a single-pass test circuit.

Parameter	Units	Target Value
Hemoglobin	g/dl	12±1
O_2 Saturation	%	65±5
pCO_2	mmHg	45±5
Base Excess	mmol/L	0±5
pH		7.4±0.1
Glucose	mg/dl	100-300
Activated Clotting Time	seconds	>480
Temperature	°C	37±2

Table 3.1: Blood Target Specifications

The performance of the M-Lung was evaluated over a range of inlet blood flow rate (Q_b) and sweep gas flow rates (Q_g). For each combination of Q_b and Q_g, a blood inlet, blood outlet, and gas outlet sample were obtained, and the inlet and outlet blood pressures were recorded. Between test intervals, the test device was flushed with 100% O_2 to prevent water condensation in the gas phase compartment of the test device. All samples were analyzed using a blood gas analyzer (ABL 800 Flex, Radiometer, Copenhagen, Denmark). The rated flow was determined as the maximum flow at which the test device outlet hemoglobin O_2 saturation was ≥95%. The O_2 transfer rate (VO_2, mL/min) at rated flow was calculated as shown in Eq. 13-15[2, 3]:

$$C_{oxy} = 13.4 \cdot tHb \cdot \frac{\%SAT}{100} + 0.0314 \cdot pO_2 \tag{13}$$

$$pO_2 = \frac{-19.7}{\left(\frac{\%SAT}{100} - 1.21\right)} \tag{14}$$

$$VO_2 = Q_b \cdot [C_{oxy\text{-}post} - C_{oxy\text{-}pre}] \quad (15)$$

Where C_{oxy} = O_2 concentration in blood (mL_{O2} L_{blood}^{-1}), tHb = hemoglobin concentration (g dL^{-1}), %SAT = hemoglobin O_2 saturation (%), Q_b = blood flow rate (L/min); $C_{oxy\text{-}post}$= post-oxygenator O_2 concentration (mL_{O2} L_{blood}^{-1}), and $C_{oxy\text{-}pre}$= pre-oxygenator O_2 concentration (mL_{O2} L_{blood}^{-1}). The CO_2 transfer rate (VCO_2, mL/min) was calculated as given in Eq. 16:

$$VCO_2 = \Delta CO_2 \cdot Q_g \cdot 1000 \quad (16)$$

Where ΔCO_2 = % CO_2 in the outlet gas sample and Q_g = sweep gas flow rate (L/min). The error bars denote the standard error of mean for each measurement.

Comparison to Commercial Devices

In order to compare the oxygen transfer efficiency of the M-Lung to similarly sized commercial devices, the following commercially available devices were used: Capiox RX05 (Terumo Corporation, Tokyo, Japan), Maquet Quadrox-i Neonatal (Gettinge Group, Rastatt, Germany), Maquet Quadrox-i Pediatric (Gettinge Group, Rastatt, Germany), Medos Hilite 1000 (Xenios AG, Heilbronn, Germany), Medos Hilite 2800 (Xenios AG, Heilbronn, Germany), Dideco D100 (Sorin Group, Milan, Italy), and Dideco D101 (Sorin Group, Milan, Italy). We obtained the maximum or rated flow (Q_{rated}) and fiber surface area (A_{fiber}) from the manufacturer manual for each of the commercial devices. The O_2 transfer at rated flow ($VO_{2\text{-}rated}$) in mL/min

was calculated using Equations 13 and 14, and the subsequent O_2 transfer efficiency ($\in_{O2}$) in mL/min/m^2 was calculated as given in Equation 17 for each device, including the M-Lung.

$$\in_{O2} = \frac{VO_{2\text{-rated}}}{A_{fiber}} \tag{17}$$

CO_2 removal is dependent on the Q_g to Q_b ratio. However, different manufacturers report CO_2 removal data for varying Q_g to Q_b ratios. In order to obtain comparable CO_2 removal data and thereby compare the CO_2 transfer efficiency of the M-Lung to similarly sized commercial devices, the CO_2 removal of each of the following commercially available devices was tested *in vitro* using the same methods as described in the previous section for the M-Lung: Capiox RX05 (Terumo Corporation, Tokyo, Japan), Medos Hilite 2800 (Xenios AG, Heilbronn, Germany), Maquet Quadrox-i Pediatric (Gettinge Group, Rastatt, Germany), and Novalung iLA (Xenios AG, Heilbronn, Germany). The CO_2 transfer efficiency ($\in_{CO2}$) for each device, including the M-Lung, was calculated for each Q_g to Q_b ratio as given in Equation 18.

$$\in_{CO2} = \frac{VCO_2}{A_{fiber}} \tag{18}$$

Results

M-Lung Performance

In *in vitro* studies, the M-Lung comprising a fiber bundle surface area of 0.28 m^2 and priming volume of 47 ml (Figure 3.4), maintained a post device oxyhemoglobin level ≥95% up to a blood flow rate of 2.0 L/min, thereby demonstrating a rated flow of 2.0 L/min (Figure 3.5). Further, the device was able to remove 200 mL/min of CO_2 at the rated blood flow rate, using a sweep gas of 16.0 L/min (Figure 3.6). The blood-side pressure drop across the M-Lung comprising a fiber bundle of porosity = 0.63 was 49 and 106 mmHg at blood flow rates of 1.0 and 2.0 L/min, respectively (Figure 3.7).

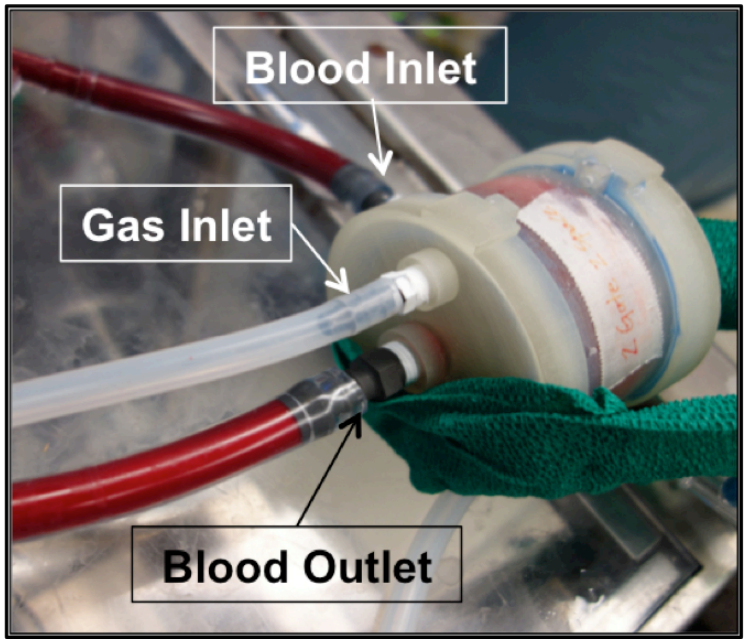

Figure 3.4: The M-Lung connected to the *in vitro* test circuit.

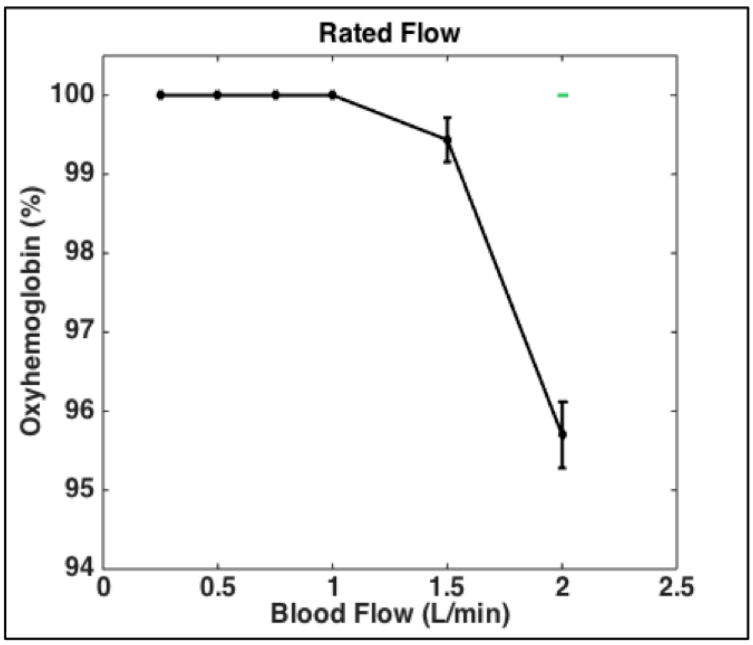

Figure 3.5: M-Lung *in vitro* oxygenation performance. The M-Lung has a rated flow of 2.0 L/min.

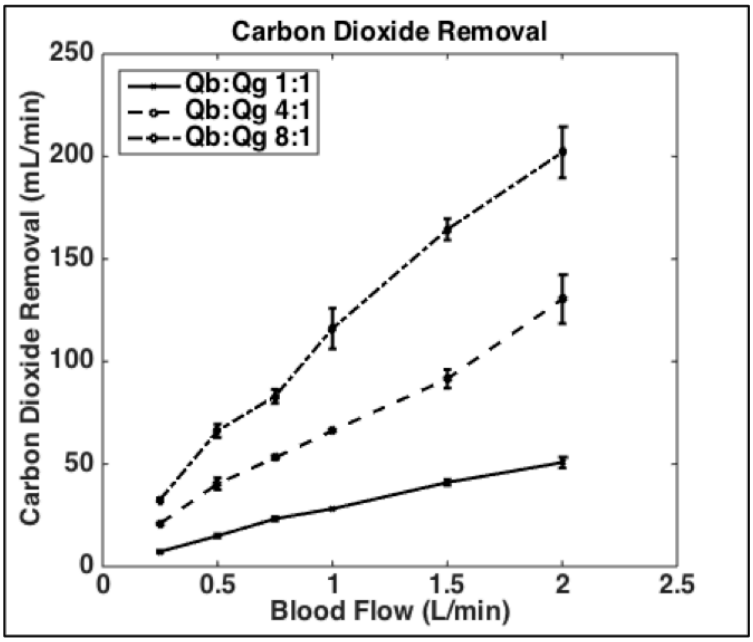

Figure 3.6: M-Lung *in vitro* CO_2 transfer performance. The M-Lung demonstrates a CO_2 clearance of 200 mL/min at the rated blood flow with a sweep gas flow rate of 16 L/min.

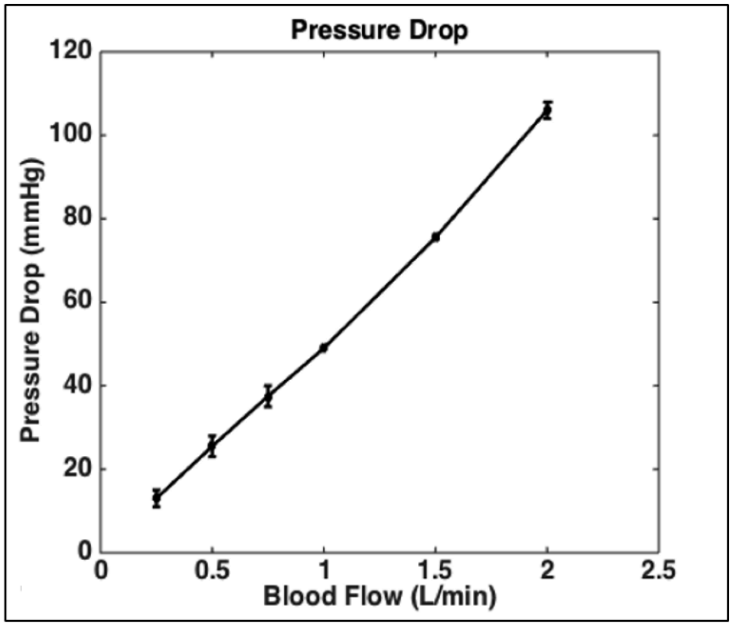

Figure 3.7. M-Lung in vitro pressure drop. The M-Lung demonstrates a pressure drop of 49 mmHg at 1.0 L/min with a fiber bundle porosity of 0.63.

Comparison to Commercial Devices

A comparison of the oxygenation transfer efficiency of the M-Lung to similarly sized commercially available devices is given in Table 3.2. The M-Lung has an oxygen transfer efficiency of 357 mL/min/m^2, which is the highest oxygen transfer efficiency of all evaluated commercial devices by ≥153 mL/min/m^2. A comparison of the CO_2 transfer efficiency of the M-Lung to similarly sized commercially available devices is given in Figure 3.7A-C. The M-Lung demonstrates one of the highest CO_2 transfer efficiencies for each of the Q_g to Q_b ratios, achieving ≥200% the CO_2 transfer efficiency of the Novalung iLA at each Q_g to Q_b ratio.

Membrane Lung	Fiber surface area (m^2)	Priming volume (mL)	Maximum or rated flow ($L\ min^{-1}$)	O_2 transfer at rated flow* ($mL_{O2}\ min^{-1}$)	O_2 transfer efficiency** ($[mL_{O2}\ min^{-1}\ m^{-2}$)
Terumo Capiox RX05	0.5	43	1.5	75	150
Maquet Quadrox-i Neonatal	0.38	40	1.5	75	197
Maquet Quadrox-i Pediatric	0.8	99	2.8	140	175
Medos Hilite 1000	0.39	57	1.0	50	128
Medos Hilite 2800	0.8	98	2.8	140	175
Sorin Dideco D100	0.22	47	0.7	35	159
Sorin Dideco D101	0.61	115	2.5	125	204
M-Lung	0.28	47	2.0	100	357

Table 3.2: Comparison of oxygen transfer efficiency of similar size membrane lungs. *Rated flow is flow of standardized venous blood at which outlet blood oxygen saturation is 95%; **O_2 transfer efficiency = O_2 transfer at rated flow (mL_{O2}/min) per fiber surface area (m^2). Data for commercial devices were obtained from manufacturer manuals for each device.

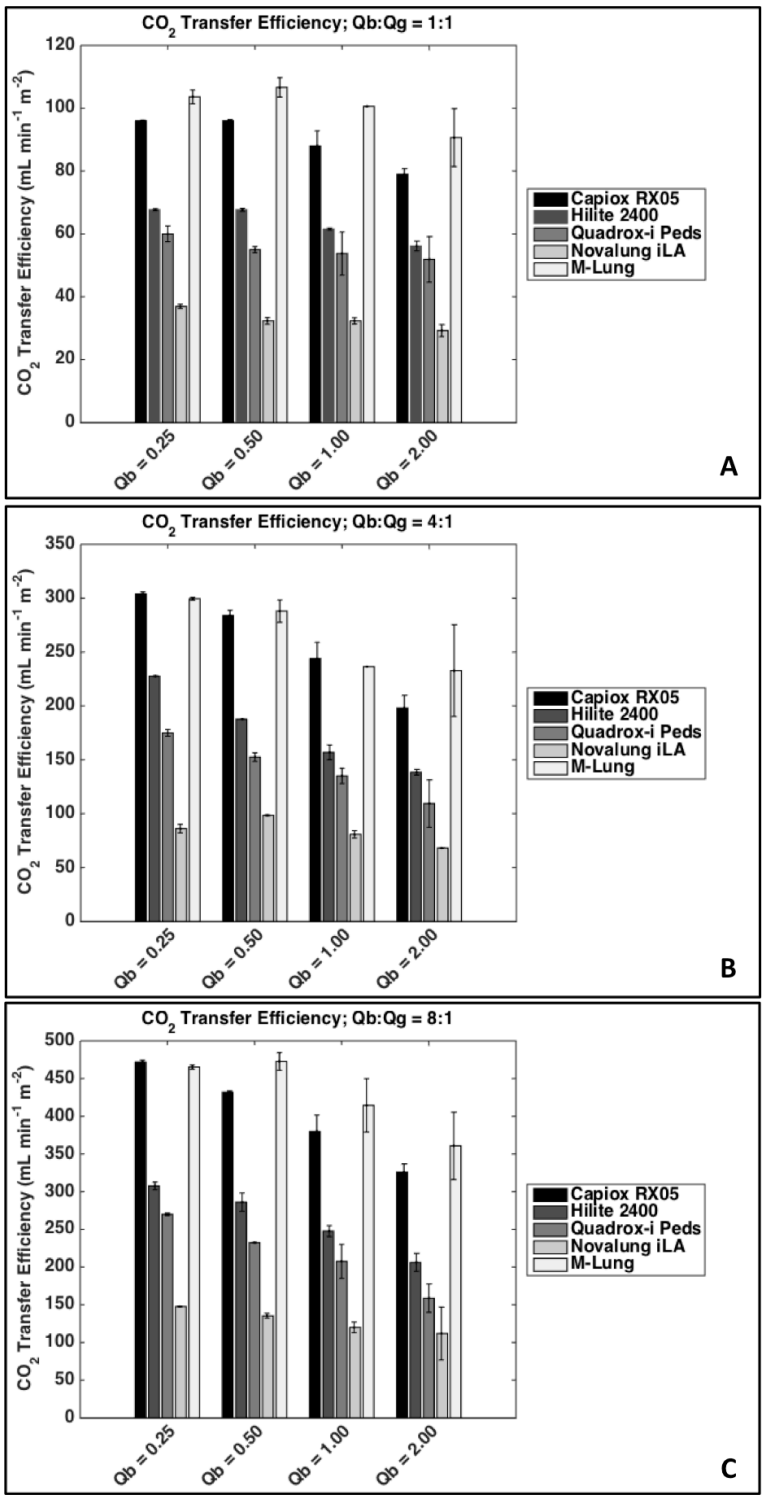

Figure 3.8: Comparison of CO_2 transfer similar size membrane lungs: A) for a Q_g to Q_b ratio of 1:1, B) for a Q_g to Q_b ratio of 4:1, and C) for a Q_g to Q_b ratio of 8:1. The Novalung iLA device has a fiber surface area of 1.3 m^2 and priming volume of 175 mL, as reported in the manufacturer manual.

Discussion

The key to maximize oxygen transfer per surface area in membrane lungs is mixing, and thereby disrupting the diffusion boundary layer, through an increase in vorticity and secondary flows.[4] Flow through circular paths will induce secondary flows to create mixing, yet a long circular spiral has high resistance. Concentric circles connected by gates created secondary flows without increasing resistance. The effect of the mixing is shown in Table 2. The oxygen transfer efficiency ($mL_{O2}/m^2\ min^{-1}$) of the M-Lung prototype is 357 $mL_{O2}/m^2\ min^{-1}$. The oxygen transfer efficiency of similar devices with predominantly straight flow path is 128-204 $mL_{O2}/m^2\ min^{-1}$.

In vitro studies demonstrate highly efficient gas exchange within the M-Lung: the device was able to maintain an oxygen saturation of ≥95% for blood flow rates up to 2.0 L/min with a fiber bundle surface area of 0.28 m^2 and priming volume of 47 ml. Further, the device was able to remove >180 mL/min of CO_2 at the rated flow. The CO_2 clearance is largely dependent on the sweep gas flow rate to blood flow rate ratio and can be further increased by increasing the sweep gas flow. The relatively short gas exchange fibers allow the M-Lung to maintain a sufficiently low gas side pressure drop at higher sweep flows and minimize water accumulation in gas phase, thereby enhancing the CO_2 removal efficiency/capacity of the device.

In comparison with similarly sized commercial devices, the M-Lung uniquely maintains one of the highest efficiencies for both oxygen and CO_2 transfer, demonstrating the effect of optimizing the lung design for overcoming both the

diffusion-limitation in oxygen transfer by means of secondary flow mixing and ventilation limitation in CO_2 transfer by means of a relatively short gas path length.

Despite its low priming volume and efficient gas exchange, the M-Lung maintains a sufficiently low blood-side pressure drop across the relevant range of blood flow rates. At a blood flow rate of 1.0 L/min, the M-Lung had a blood-side pressure drop <50 mmHg, which is within the range supported by a systemic arterio-venous pressure gradient. At its rated flow of 2.0 L/min, the M-Lung had a pressure drop of 106 mmHg, which is well within the range supported by a blood pump. A comparison of the simulations in Chapter 2 and experimental pressure drop across the M-Lung suggests a fiber bundle permeability of $2.8e^{-9}$ m^2 for the current M-Lung configuration.

References

1. Guidance for Cardiopulmonary Bypass Oxygenators 510(k) Submissions; Final Guidance for Industry and FDA Staff [Internet]. Food and Drug Administration. 2000 [cited October 1, 2016]. Available from: http://www.fda.gov/MedicalDevices/DeviceRegulationandGuidance/GuidanceDocuments/ucm073668.htm.

2. Bartlett RH. Physiology of Gas Exchange During ECMO for Respiratory Failure. Journal of intensive care medicine. 2016.

3. Benn JA, Drinker PA, Mikic B, Shults MC, Lacava EJ, Kopf GS, et al. Predictive Correlation of Oxygen and Carbon Dioxide Transfer in a Blood Oxygenator with Induced Secondary Flows. T Am Soc Art Int Org. 1971;17(Apr):317-&.

4. Zwischenberger JB, Anderson CM, Cook KE, Lick SD, Mockros LF, Bartlett RH. Development of an implantable artificial lung: challenges and progress. ASAIO journal. 2001;47(4):316-20.

Chapter 4

Conclusion

Conclusions

In conclusion, using CFD and optical flow visualization methods we designed a unique hollow fiber membrane lung based on concentric circular blood flow paths connected by gates, referred to as the M-Lung. Based on these analyses, the optimal M-Lung design was prototyped and tested *in vitro* in accordance with regulatory guidelines. The performance and efficiency of the M-Lung was then compared to similarly sized commercially available devices in order to evaluate the effectiveness of our design. Based on these studies, it can be concluded that:

1. The concentric circular blood flow paths connected by gates result in increased secondary flow mixing within the M-Lung housing; similar vortex formation was observed in both computational and experimental methods.
2. The circular design minimizes stagnant regions and results in a well distributed flow profile.
3. Increasing the number of gates results in a longer blood path and cumulative mixing at the cost of an increased pressure drop and resistance across the device.

4. In an optimized M-Lung housing, the incorporation of the fiber bundle results in a significant increase of pressure drop and dampening of secondary flow mixing. However, the magnitude of these effects can be minimized by increasing the permeability and porosity of the fiber bundle, at the cost of a reduced fiber surface area and increased priming volume.
5. The M-Lung comprises a fiber surface area of 0.28 m^2 and priming volume of 47 mL.
6. The M-Lung has rated flow of 2 L/min and a CO_2 clearance of 200 mL/min at the rated blood flow.
7. The blood-side pressure drop of the M-Lung is <50 mmHg at a blood flow rate of 1.0 L/min, which is within the range supported by a systemic arterio-venous pressure gradient. At its rated flow of 2.0 L/min, the M-Lung had a pressure drop of 106 mmHg, which is well within the range supported by a blood pump.
8. The M-Lung has an oxygenation efficiency of 357 mL/min/m^2 and CO_2 clearance efficiency that is more than 2 times that of the Novalung iLA (a commercial lung designed for CO_2 clearance). In comparison with similarly sized commercial devices, the M-Lung uniquely maintains one of the highest efficiencies for both oxygen and CO_2 transfer.

This M-Lung design meets the functional requirements for providing systemic CO_2 removal support in adults as well as total respiratory support for infants and small children; in addition to sufficient gas transfer, it comprises a low priming volume, allowing for minimal hemodilution and rapid transit time. The rapid transit time at rated

flow and the absence of corners where blood can stagnate should minimize thrombogenicity. Furthermore, given its compact size, controllable resistance, and potential for low thrombogenicity, the M-Lung has potential for providing long-term ambulatory respiratory support, in arterio-venous mode for clearance of CO_2 for patients with end-stage COPD or pulmonary artery to left atrium mode for total lung support.

Future Work

Future work will evaluate the performance of a clinical M-Lung in an *in vivo* model to further assess its biocompatibility and chronic performance. Using a disease animal model, the chronic performance and efficacy of the M-Lung could be evaluated in treating the pathophysiology of end-stage lung disease.

Future studies will also investigate the incorporation of antithrombogenic materials such as nitric oxide (NO), which minimizes platelet adhesion and activation, coupled with argatroban, which is a direct thrombin inhibitor, in the M-Lung housing and sweep gas in an effort to eliminate systemic anticoagulation.

The M-Lung design could be scaled up to achieve total adult respiratory support. Scaling up to adult size devices will be done with a return to CFD and PIV to optimize the properties of a device with a 5 L/min rated flow, pressure drop <60 mmHg at rated flow, and CO_2 transfer 2 times oxygen transfer at rated flow. We expect that this will require 0.6 to 0.8 m^2 of gas transfer surface, in contrast with current adult devices, which comprise 1.5-1.8 m^2.